

Available online at [www.sciencedirect.com](http://www.sciencedirect.com)

ScienceDirect

journal homepage: [www.elsevier.com/locate/he](http://www.elsevier.com/locate/he)

# A fault diagnosis model for proton exchange membrane fuel cell based on impedance identification with differential evolution algorithm

Runben Du<sup>a,c</sup>, Xuezhe Wei<sup>a,c</sup>, Xueyuan Wang<sup>b,c</sup>, Siqi Chen<sup>a,c</sup>,  
Hao Yuan<sup>a,c</sup>, Haifeng Dai<sup>a,c,\*</sup>, Pingwen Ming<sup>a,c</sup>

<sup>a</sup> School of Automotive Studies, Tongji University, No. 4800 Caoan Road, Shanghai, 201804, China

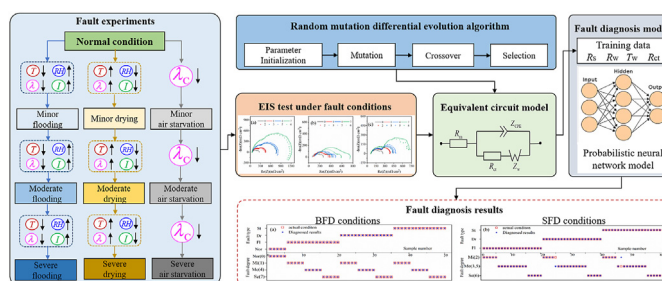
<sup>b</sup> Department of Control Science and Engineering, Tongji University, No. 4800 Caoan Road, Shanghai, 201804, China

<sup>c</sup> National Fuel Cell Vehicle & Powertrain System Research & Engineering Center, No. 4800, Caoan Road, Shanghai, 201804, China

## HIGHLIGHTS

- A RMDE algorithm is proposed to realize the impedance parameter identification.
- A fault diagnosis model based on the probabilistic neural network is developed.
- The diagnosis accuracies for fault type and fault degree reach 100% and 96.67%.

## GRAPHICAL ABSTRACT



## ARTICLE INFO

### Article history:

Received 4 May 2021

Received in revised form

9 September 2021

Accepted 13 September 2021

Available online 2 October 2021

### Keywords:

Fuel cell

Random mutation differential evolution

Parameter identification

Fault diagnosis

Probabilistic neural network

## ABSTRACT

An effective online fault diagnosis system is of great significance to improve the reliability of fuel cell vehicles. In this paper, a fault diagnosis model for proton exchange membrane fuel cells is proposed. Firstly, the tests of electrochemical impedance spectroscopy under different fault types (flooding, drying, air starvation) and fault degrees (minor, moderate, severe) are carried out, and each polarization loss of the fuel cell is denoted by an equivalent circuit model (ECM). Then, the parameters of the ECM are identified by the proposed random mutation differential evolution algorithm. Furthermore, the parameters identified under different fault conditions are used to train and test a probabilistic neural network-based fault diagnosis model. The fault diagnosis model achieves diagnosis accuracies of 100% for the fault type and 96.67% for the fault degree. By setting operating conditions with different fault degrees, the fault diagnosis model proposed in this paper can realize the fault type and fault degree diagnosis, effectively avoiding the misjudgment of fault types, and is effective for improving the reliability of the fuel cell system.

© 2021 Hydrogen Energy Publications LLC. Published by Elsevier Ltd. All rights reserved.

\* Corresponding author. School of Automotive Studies, Tongji University, No. 4800 Caoan Road, Shanghai, 201804, China.

E-mail address: [tongjidai@tongji.edu.cn](mailto:tongjidai@tongji.edu.cn) (H. Dai).

<https://doi.org/10.1016/j.ijhydene.2021.09.126>

0360-3199/© 2021 Hydrogen Energy Publications LLC. Published by Elsevier Ltd. All rights reserved.

## Introduction

The growing car ownership and accelerated consumption of fossil fuels force the automotive industry to develop new energy vehicles (NEVs). Fuel cell vehicles (FCVs) are deemed to be a promising direction considering the characteristics of long driving range and short refueling time [1]. Due to the suitable operating temperature and short startup time, proton exchange membrane fuel cells (PEMFCs) have become the most commonly used fuel cell type in vehicular scenarios. However, the reliability still demands significant strengthening before large-scale commercialization [2,3].

Developing an online fault diagnosis system is an efficacious approach to relieve the problems mentioned above. Information acquisition tools and fault diagnosis methods are the two primary parts of a fault diagnosis system [4]. Generally, information acquisition tools can be divided into electrochemical-based tools and physical-chemical-based tools [5,6]. Polarization curve, current pulse injection, electrochemical impedance spectroscopy (EIS) and cyclic voltammetry are several common electrochemical-based tools, of which EIS is the most popular diagnostic tool due to the ability to separate the electrochemical processes inside the fuel cell [7,8]. Seyed et al. [9] investigated the impacts of hydrogen and air stoichiometry on reactant starvation and discovered that lower air stoichiometry could inflate the middle-frequency and low-frequency impedance arc. In Ref. [10], air velocities matched by impedance tested under various air stoichiometries at an extensive range of current density was applied as an online reactant starvation diagnostic tool. Hink et al. [11] employed EIS to observe the Nafion® membranes of the fuel cell and found that the performance of the electrolyte membrane was determined by the Ohmic resistance and the diffusion parameters. Besides, it should be emphasized that unlike other physical-chemical-based diagnosis tools, such as X-ray [12], gas chromatography [13], and neutron imaging [14], the impedance spectrum at a wide range of frequencies can be obtained in the actual vehicular environment by numerous fast impedance acquisition approach with low implementation cost. Hong et al. [15] integrated an AC excitation device in a DC/DC converter, which is superimposed with the DC signal to the stack for impedance calculation. The experimental results in a vehicular fuel cell system indicated that the calculated impedance at selected 320 Hz could be a valuable indicator for membrane water content detection. This approach requires only additional excitation and sampling devices and has been adopted by Toyota Mirai to obtain high frequency resistant for shutdown purge and cold start control [16].

On the other hand, the fault diagnosis methods for fuel cells can be classified into two categories: (i) model-based method; (ii) non-model-based method [17,18]. The model-based fault diagnosis method simulates the internal state of the fuel cells by establishing an empirical model or a mechanism model [19]. Then, the work of fault diagnosis is carried out by analyzing the residual between the output of the model

and the actual physical system, which emphasizes the importance of the model accuracy. The mechanism models are a series of spatial differential equations based on the Nernst-Planck equation, the Butler-Volmer equation and Fick's law to simulate the internal state of the fuel cell [20]. These models usually have high accuracy, while the high computational complexity makes them unsuitable for online applications. The empirical models are constructed based on prior knowledge and use empirical formulas or analogue circuits to replace the complex mathematical equations, including equivalent circuit models (ECMs), observer-based models and parity space models, which reach a compromise in terms of computational complexity and accuracy. Rubio et al. [21] proposed two types of ECMs for EIS fitting under three fault conditions, and the relationships between the ECM parameters and electrochemical parameters are investigated. Yuan et al. [22] built a nonlinear internal state observer to estimate the mass flow of oxygen and nitrogen of a vehicular PEMFC system and got acceptable results. Buchholz et al. [23] proposed a parity-space approach for online fault diagnosis to linearize the system in a discrete subspace. These methods have become the dominant methods in fault diagnosis due to the availability of different kinds of sensors employed in the fuel cell control system.

Instead of exploring the internal state, the non-model-based fault diagnosis methods determine the fault state of the target system based on large amounts of historical data [24,25]. Li et al. [26] proposed an online fault diagnosis method, which utilized the multiple-class support vector machine to classify the fuel cell faults, and the results were proved to be acceptable both offline and online. Pahon et al. [27] employed the energy contained in each detail of the wavelet decomposition to diagnose whether the fuel cell system was under the over air stoichiometry state. These methods are applicable for nonlinear systems such as fuel cells, but the diagnosis results are highly dependent on real-time test data. Recently, several researchers have combined EIS and non-model-based diagnostic methods for fuel cell faults diagnosis. Lu et al. [28] designed an online fault diagnosis system. Firstly, the impedance spectrum was obtained online, and the nonlinear least squares (NLS) algorithm was used to identify the ECM parameters. Then, the parameters were fed into a support vector machine-based model for fault diagnosis. The diagnostic accuracy was 90.90% (20/22), where one normal condition was misclassified as a drying fault, and another flooding fault was misclassified as a drying fault. Wang et al. [29] adopted a similar research idea, but the whole research was based on the simulation data from the proposed fuel cell model, lacking the experimental verification.

There are still some problems that existed in previous studies. Firstly, the identification process was usually based on the least square (LS) class methods or directly employing the fitting software [30,31]. These kinds of methods have fast convergence speed, but the accuracy of the identified parameters is vulnerable to the selected initial value [32], making them inappropriate for fault diagnosis in real applications. Furthermore, previous studies simply divided the faults into

several types, such as flooding and drying. Once the fault type is incorrectly identified, the controller in the vehicular fuel cell system will take the wrong measures to exacerbate the fault degree and even have an irreversible impact on the fuel cell. Finally, the test data and training data input to the diagnosis model are obtained under the same working conditions with almost identical characteristics. Therefore, it is easy to get a high diagnostic accuracy when test the model with the data. However, vehicular fuel cell systems operating under dynamic conditions have been facing a wide variety of conditions with different fault types/degrees. As a result, the diagnostic models trained under specific fault conditions are challenging to maintain high diagnostic accuracies in practical applications.

Aiming at the problems mentioned above, a fault diagnosis model for the PEMFCs is proposed in this paper. First of all, a random mutation differential evolution (RMDE) algorithm is proposed to identify the parameters in an improved Randles ECM, and a large enough parameter range can be employed to replace the accurate initial parameter values in LS class algorithms. Furthermore, a probabilistic neural network-based fault diagnosis model trained with the identified ECM parameters is proposed to solve the fault type confusion. This method can further diagnose the fault degree on the basis of the fault type. Finally, four subdivided fault degree (SFD) conditions are designed between three basic fault degree (BFD) conditions to test the diagnosis performance of the model under arbitrary fault conditions.

## Differential evolution algorithm applied to impedance parameter identification

### Establishment of the Randles ECM

Randles ECM is a commonly used ECM in fuel cells impedance fitting, as it balances model complexity and fitting accuracy. Fig. 1 shows the structure of two common Randles ECMs and their fitting results obtained by Zview (a mature impedance fitting software developed by Scribner Associates Inc). The external operating parameters of the fuel cell for the EIS measurement are recommended by the manufacturer

(temperature  $T = 75\text{ }^{\circ}\text{C}$ , current density  $I = 1\text{ A/cm}^2$ , back-pressure  $P_C/P_A = 150/160\text{ kPa}$ , relative humidity  $RH_C/RH_A = 50\%/60\%$ , stoichiometry  $\lambda_C/\lambda_A = 2.5/1.5$ ). It can be seen from the figure that the chi-square in Fig. 1(b) is relatively low, indicating that the ECM in the figure has a better fitting capability. The high-frequency part of fuel cells impedance spectrum is commonly a compressed semicircle rather than a standard semicircle [33]. A constant phase element (CPE) that can change the compression degree of the semicircle is utilized in Fig. 1(b) to replace the standard capacitor, thus obtaining a better fitting result. The expression for CPE in is shown in Eq. (1).

$$Z_{CPE} = \frac{1}{T_{dl} \cdot (j\omega)^{P_{dl}}} \quad (1)$$

where  $P_{dl}$  represents the CPE exponent (When  $P_{dl} = 1$ , it is a standard capacitor);  $T_{dl}$  represents the pseudo-capacitance. Besides, the charge transfer impedance  $R_{ct}$  in the ECM, corresponding to the high frequency of the impedance spectrum, is mainly caused by the slow reaction of oxygen reduction velocity at the cathode. The ohmic impedance  $R_s$ , equaling to the intercept of the impedance spectrum and the real axis, is caused by the resistance of electrons passing through the electrode material and hydrogen ions passing through the proton exchange membrane. The Warburg diffusion element  $Z_w$ , corresponding to the low frequency of the impedance spectrum, provides a measure of the mass transport losses that occurred in the cathode flow field and gas diffusion layer. According to the Butler–Volmer equation and Fick's second diffusion law, the general expression of  $Z_w$  could be derived [34]:

$$Z_w = \frac{RT}{n^2 F^2 S \sqrt{j\omega}} \frac{\tanh \sqrt{j\omega/D} \delta}{C \sqrt{D}} \quad (2)$$

Eq. (2) can be re-written as:

$$Z_w = \frac{RT}{n^2 F^2 S \sqrt{j\omega}} \frac{1}{C} \frac{1}{D} \delta \frac{\tanh \sqrt{j\omega(\delta^2/D)}}{\sqrt{\delta^2/D}} \quad (3)$$

Which leads to the definition of two parameters, a time constant

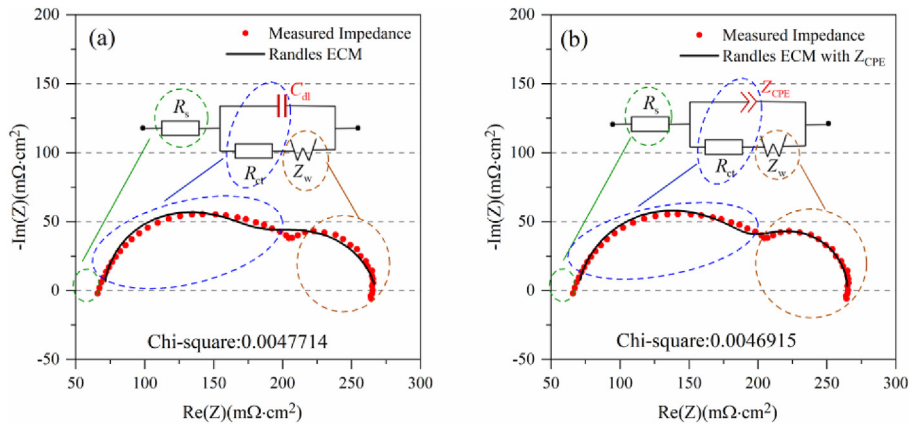


Fig. 1 – Impedance spectrum fitting results of (a) the Randles ECM and (b) the Randles ECM with  $Z_{CPE}$ .

$$T_w = \frac{\delta^2}{D} \quad (4)$$

And a resistance

$$R_w = \frac{RT\delta}{n^2 F^2 SCD} \quad (5)$$

This leads to the expression of  $Z_w$ :

$$Z_w = R_w \frac{\tanh \sqrt{T_w j \omega}}{\sqrt{T_w j \omega}} \quad (6)$$

Generally, the curvature of the low frequency part of the fuel cell impedance spectrum is not a constant value. Setting the exponent term of  $T_w j \omega$  as an adjustable parameter can adjust the curvature of its frequency response characteristics, making the model have a better fitting performance [35]. Therefore, the final expression of  $Z_w$  is:

$$Z_w = R_w \frac{\tanh(T_w j \omega)^{P_w}}{(T_w j \omega)^{P_w}} \quad (7)$$

where  $P_w$  represents the adjustable exponential parameter of the Warburg element.

The total impedance expression for the Randles ECM with  $Z_{CPE}$  in Fig. 1(b) can be described as Eq. (8).

$$Z = R_s + \frac{Z_{CPE} \cdot (R_{ct} + Z_w)}{Z_{CPE} + R_{ct} + Z_w} \quad (8)$$

where  $R_s, R_w, T_w, \dots, R_{ct}, T_{dl}, P_{dl}$  are the seven parameters to be identified.

#### Parameter identification based on the RMDE algorithm

Compared with the LS class methods, intelligent optimization algorithms are more appropriate for online optimization while are rarely employed in impedance parameter identification. Wang et al. [36] adopted the particle swarm optimization algorithm to search the initial values of the parameters in a lithium battery ECM, while the final parameter values were still identified by Zview, which did not automate the whole identification process. This paper puts forward an RMDE algorithm based on the differential evolution (DE) algorithm to realize the whole process of parameter identification.

#### Determination of the parameter range in the ECM

The range of the parameters in the ECM listed in Table 1 is obtained by referring to relevant literature and expanding the

range of the offline parameter identification results, which is large enough to cover all operating conditions of fuel cells.

#### Parameter identification based on the RMDE algorithm

##### Step 1 Population initialization and fitness function determination

$$\begin{aligned} D &= 7 \quad N = 70 \\ k_{\max} &= 500 \quad E = 0.001 \end{aligned} \quad (9)$$

where  $D$  represents the individual dimension, which equals the parameter numbers in the ECM;  $N$  represents the individual numbers in the population;  $k_{\max}$  represents the preset maximum iterations times;  $E$  represents the error criterion.

The fitness function providing a measure to evaluate the merits of individuals in the population is described as follow:

$$\begin{cases} F = \sum_{j=1}^n (W_j [(Z_j - z_j) + (Z'_j - z'_j)^2]) \\ W_j = \frac{1}{Z_j^2 + Z'^2_j} \end{cases} \quad (10)$$

where  $n$  represents the number of frequency points in the EIS;  $Z_j$  and  $Z'_j$  represent the real part and imaginary part of the measured impedance spectrum, respectively;  $z_j$  and  $z'_j$  represent the real part and imaginary part of the impedance spectrum calculated by the RMDE algorithm, respectively. The weight factor  $W_j$  considering the impedance modulus is introduced here to normalize the errors between the measured EIS and the calculated EIS.

##### Step 2 Individual initialization

$$X_i^0 = \text{rand} \cdot (X_{\max} - X_{\min}) + X_{\min} \quad i = 1, 2, 3, \dots, N \quad (11)$$

where  $X_i^0 \in R^{1 \times D}$  represents the target vector of the  $i^{\text{th}}$  individual at generation 0,  $\text{rand}$  is a random number that obeys a uniform distribution within the range of  $[0, 1]$ ;  $X_{\max}$ ,  $X_{\min} \in R^{1 \times D}$  represent the upper and lower bounds vectors, whose values are determined by the data listed in Table 1.

##### Step 3 Mutation operation

This paper proposed a random mutation differential strategy based on the two commonly used differential strategies (DE/rand/1, DE/best/1) [37] to strike a balance between global search capability and local identification accuracy of the algorithm, which is described as Eq. (12).

$$V_i^k = \begin{cases} X_{\text{best}}^k + \text{rand} \cdot (X_{p2}^k - X_{p3}^k) & \text{if } \text{rand} > 0.5 \\ X_{p1}^k + \text{rand} \cdot (X_{p2}^k - X_{p3}^k) & \text{if } \text{rand} \leq 0.5 \end{cases} \quad (12)$$

where  $V_i^k \in R^{1 \times D}$  represents the mutant vector;  $X_{p1}^k, X_{p2}^k, X_{p3}^k$  represent the three target vectors randomly selected in the population, and  $i \neq p1 \neq p2 \neq p3$ ;  $X_{\text{best}}^k$  represents the target vector with the smallest fitness value.

**Table 1 – Parameter range in the ECM.**

Symbol	Unit	Range
$R_s$	$\text{m}\Omega \cdot \text{cm}^2$	10–200
$R_w$	$\text{m}\Omega \cdot \text{cm}^2$	10–2000
$T_w$	$\text{s}^{P_w} / (\text{m}\Omega \cdot \text{cm}^2)$	0.1–1 [34]
$P_w$	/	0.5–1 [34]
$R_{ct}$	$\text{m}\Omega \cdot \text{cm}^2$	100–1000
$T_{dl}$	$\text{s}^{P_{dl}} / (\text{m}\Omega \cdot \text{cm}^2)$	$1 \times 10^{-5} \sim 1 \times 10^{-4}$
$P_{dl}$	/	0.5–1 [33]



#### Step 4 Crossover operation

$$u_{ij}^k = \begin{cases} v_{ij}^k, & \text{rand} \leq CR \text{ or } j = j_{\text{rand}} \\ x_{ij}^k, & \text{else} \end{cases} \quad (13)$$

where  $x_{ij}^k$ ,  $v_{ij}^k$  and  $u_{ij}^k$  represent the  $j^{\text{th}}$  element of  $\mathbf{X}_i^k$ ,  $\mathbf{V}_i^k$  and  $\mathbf{U}_i^k$ , respectively;  $CR \in (0, 1)$  represents the preset crossover probability;  $j_{\text{rand}}$  represents a random integer selected in  $[1, 2, 3, \dots, D]$ .

An exponential adjustment method for CR expressed in Eq. (14) is proposed, enabling CR to have a relatively small magnitude at the beginning of the iteration to strengthen the algorithm's global search capability. As iteration progresses, CR gradually approaches  $CR_{\text{max}}$ , which guarantees the excellent local exploration performance of the algorithm at the end of the iteration [38,39].

$$CR(k) = CR_{\text{min}} \left( \frac{CR_{\text{max}}}{CR_{\text{min}}} \right)^{\frac{k}{k_{\text{max}}}} \quad (14)$$

where  $CR_{\text{max}} = 0.8$ ,  $CR_{\text{min}} = 0.2$ .

#### Step 5 Selection option

$$\mathbf{X}_i^{k+1} = \begin{cases} \mathbf{U}_i^k, & \text{if } E(\mathbf{U}_i^k) < E(\mathbf{X}_i^k) \\ \mathbf{X}_i^k, & \text{else} \end{cases} \quad (15)$$

where  $E(\mathbf{U}_i^k)$  and  $E(\mathbf{X}_i^k)$  are the fitness values of  $\mathbf{U}_i^k$  and  $\mathbf{X}_i^k$ , respectively.

#### Step 6 Verification of compliance with closing conditions

Perform the next iteration or jump out the iteration after reaching the error criterion  $E$ .

### Experimental platform

In the research, a membrane electrode assembly (MEA) with a reaction area of 50 cm<sup>2</sup> produced by Greenlight Innovation is tested. The MEA is sandwiched between two graphite bipolar plates by a special fixture for the fuel cell. Due to the slight temperature gradient in the direction perpendicular to the fuel cell, the temperature of the coolant flowing through the fuel cell is regarded as the whole-cell temperature. Fig. 2 shows the experimental schematic diagram of the entire test system. The experiments are conducted on a Greenlight G60 with a rated power of 500 W. The test bench includes five inlet pipes to provide the required reaction gases and coolant (hydrogen, air, nitrogen, deionized water and coolant), while the waste accompanied with the reaction is drained through the corresponding exhaust pipes. The mass flow of air and hydrogen is precisely controlled by the dynamically adjusted mass flow controllers (MFC). Meanwhile, the pressure of the reactant in the fuel cell can be regulated in real-time by adjusting the opening of the proportional valves in the backpressure control

module. Because hydrogen and air are bubbling humidified, the temperature of deionized water in the humidifiers can be regarded as the dew point temperature. Then, the reactant humidity can be dynamically adjusted by controlling the difference between the dew point temperature and the intake reactant temperature. Besides, this test bench includes an electronic load and a frequency response analyzer (FRA: Reference 3000AE with 30 k Booster, Gamry Instruments, America). The impedance spectra are recorded by sweeping frequencies over the range of 1 kHz to 100 mHz with 12 points per decade. The amplitude of the excitation current is set to 8% of the amplitude of the operating current. In addition, a host computer with Intel i5-10210U CPU and 16 GB RAM is utilized to run the RMDE algorithm program developed by MATLAB.

Based on the test bench, the external operating parameters of the fuel cell, such as temperature  $T$ , current density  $I$ , backpressure  $P_A/P_C$ , relative humidity  $RH_A/RH_C$ , and stoichiometry  $\lambda_C/\lambda_A$ , can be controlled precisely. As shown in Table 2, four different operating conditions of the fuel cell are conducted to test the identification performance of the RMDE algorithm. Condition 1 is the optimal operating condition of the fuel cell recommended by the manufacturer, and the other three conditions are artificially set by changing part of the operating parameters on the basis of the recommended condition.

### Discussion of the parameter identification results

#### Parameter identification accuracy

Fig. 3 depicts the impedance spectra under the four conditions fitted by the RMDE algorithm and Zview. The fitting results of the RMDE algorithm basically coincide with those of Zview. Besides, it is worth noting that some inductive components appear in the low-frequency portion (<0.2 Hz) of the impedance spectra in Fig. 3(a), (b), (c). Pivac et al. [40] provided several possible causes for this phenomenon, such as side reactions with intermediate species, carbon monoxide poisoning and water transport. However, the interpretation of the inductive features is still ambiguous. Therefore, the ECM presented in subsection 2.1 does not consider the low-frequency inductive components of the impedance spectra, which is assumed to be the dominant reason for the fitting errors.

To further explore the identification accuracy of the RMDE algorithm, Table 3 quantitatively compares the identification results achieved by the RMDE algorithm and Zview. The seven parameters identified by the two methods are on the same order of magnitude, and the relative error is within 4.5%, indicating that the proposed algorithm is accurate enough for impedance parameter identification.

#### The stability and convergence speed of the RMDE algorithm

Apart from high fitting accuracy, an available identification algorithm for onboard applications also demands strong stability and fast convergence speed. In this paper, the algorithm was executed ten times in succession, and the algorithm stability is expressed through the fitness value variation. The

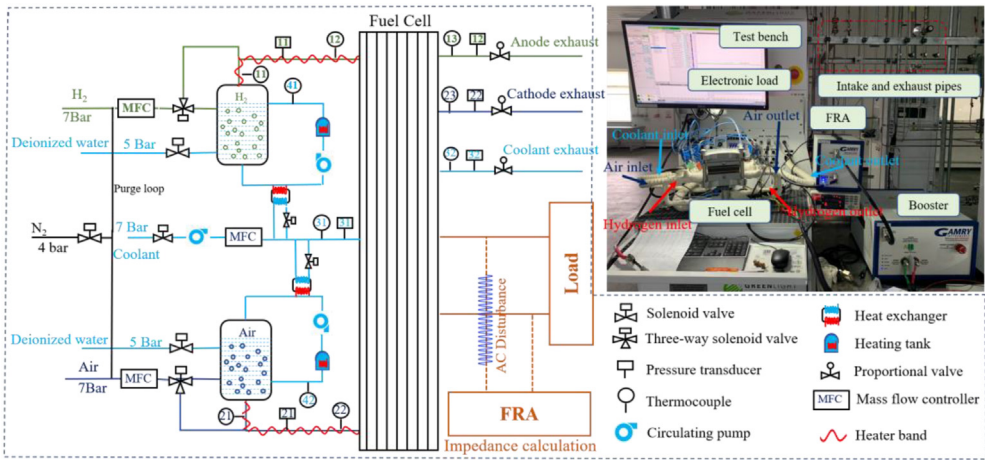


Fig. 2 – Experimental schematic diagram of the fuel cell test system.

Table 2 – External operating parameters of the fuel cell.					
Conditions	$I$ (A/cm <sup>2</sup> )	$P_C/P_A$ (kPa)	$T$ (°C)	$\lambda_C/\lambda_A$	$RH_C/RH_A$
1	1	150/160	75	2.5/1.5	50%/60%
2	1.7	150/160	55	1.7/1.5	90%/90%
3	0.3	150/160	85	3/1.5	0%/50%
4	1	150/160	75	1.2/1.5	50%/60%

fitness values of the four conditions can converge to their respective stable values in the course of all ten times executions: 0.0684 (Condition 1), 0.305 (Condition 2), 0.0115 (Condition 3), and 0.1167 (Condition 4), demonstrating the excellent stability of the RMDE algorithm. Analyzing the fitness values from different working conditions, the fitness value of condition 2 is the maximum among all conditions, and condition

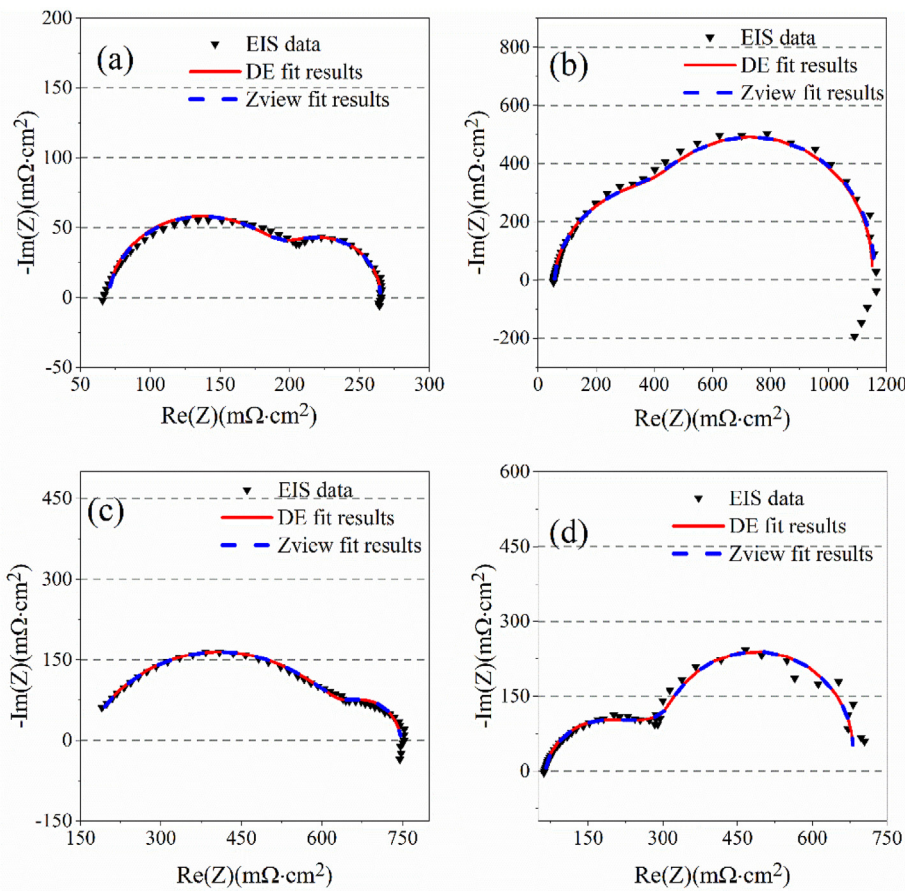


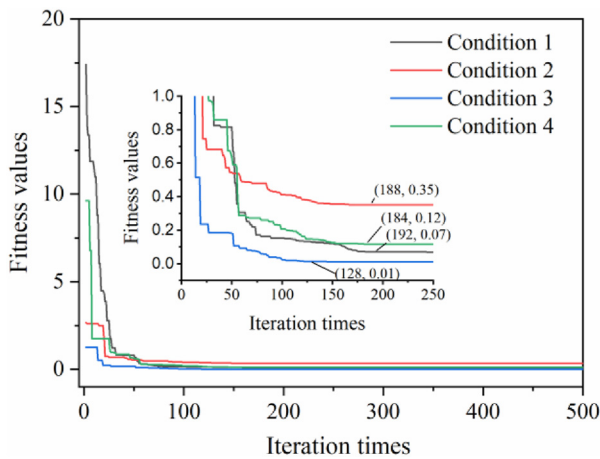
Fig. 3 – EIS fitting results of the RMDE algorithm and Zview under four working conditions: (a) Condition 1; (b) Condition 2; (c) Condition 3; (d) Condition 4.

**Table 3 – Parameter identification results of the RMDE algorithm and Zview.**

Conditions	Data type	$R_s$	$R_w$	$T_w$	$P_w$	$R_p$	$T_{dl}$	$P_{dl}$
1	RMDE	69.31	75.16	0.15	0.51	120.75	3.46E-05	0.93
	Zview	69.61	73.49	0.15	0.51	121.88	3.62E-05	0.92
	Error/%	0.43	2.27	0.00	0.00	0.93	4.42	1.09
2	RMDE	57.13	517.43	0.17	0.62	575.16	4.58E-05	0.97
	Zview	57.49	525.81	0.17	0.61	574.13	4.63E-5	0.96
	Error/%	0.63	1.59	0.00	1.64	0.18	1.08	1.04
3	RMDE	159.05	104.99	0.21	0.54	483.32	1.70E-05	0.75
	Zview	158.90	105.40	0.21	0.53	483.50	1.71E-5	0.75
	Error/%	0.09	0.39	0.00	1.89	0.04	0.58	0.00
4	RMDE	65.32	414.82	0.53	0.58	198.29	4.08E-05	0.93
	Zview	65.67	412.90	0.53	0.58	200.10	4.20E-5	0.93
	Error/%	0.53	0.47	0.00	0.00	0.90	2.86	0.00

2 also has the most significant inductive components in the low-frequency EIS (<0.2 Hz), which proves the conclusion that the fitting errors mainly come from the low-frequency inductive component. Furthermore, due to the extremely small cathode stoichiometry  $\lambda_c$  in condition 4, the low-frequency part of the EIS (<1 Hz) began to show a nonlinear relationship, which is the main reason for the fitting errors. Both the high-frequency and low-frequency parts of the EIS in condition 1 exhibit fitting errors, but the impedance modulus is relatively small. Thus a relatively small fitness value is obtained. In condition 3, the EIS fitting error also mainly come from the low-frequency part, but the inductive impedance component is not apparent, which is the condition with the smallest fitness value among the four conditions.

Fig. 4 shows the variation of the fitness function with the iteration times. The fitness values of all conditions converged to a stable value after 200 iterations. When maximum iterations times  $k_{max}$  was changed to 200, the corresponding fitness values were respectively changed to 0.0691(Condition 1), 0.3051(Condition 2), 0.0142(Condition 3), 0.1171(Condition 4). Compared with Zview, the parameter identification error was kept within 5%, but the corresponding convergence time was reduced from 7s to 3s, significantly enhancing system efficiency.

**Fig. 4 – Convergence curve of fitness values under the four conditions.**

## Fault diagnosis based on the probabilistic neural network

### Principle of the probabilistic neural network

After verifying the effectiveness of the RMDE algorithm, the identified parameters can be fed into a probabilistic neural network-based fault diagnosis model for fault diagnosis. The probabilistic neural network is a kind of tutor-learning neural network, which needs to be provided with a series of input data and expected output data (training sample pair) during the model training phase. Fig. 5 shows a schematic diagram of the probabilistic neural network, consisting of an input layer, a hidden layer, and an output layer.

The calculation process is as follows:

#### 1) Training sample pair initialization

$$P = \begin{bmatrix} p_{11} & p_{12} & \cdots & p_{1Q} \\ p_{21} & p_{22} & \cdots & p_{2Q} \\ \vdots & \vdots & \ddots & \vdots \\ p_{R1} & p_{R2} & \cdots & p_{RQ} \end{bmatrix}, T = \begin{bmatrix} t_{11} & t_{12} & \cdots & t_{1Q} \\ t_{21} & t_{22} & \cdots & t_{2Q} \\ \vdots & \vdots & \ddots & \vdots \\ t_{K1} & t_{K2} & \cdots & t_{KQ} \end{bmatrix} \quad (16)$$

where  $P$  represents the input sample, which is composed of the identified parameters in the ECM;  $T$  represents the output sample, which is composed of the fault codes denoted by different Arabic numerals;  $Q$  represents the sample numbers;  $R$  represents the dimension of the input sample, i.e., the number of the feature parameters;  $K$  represents the dimension of the output variable, corresponding to the number of fault codes.

#### 2) Radial basis function mapping

The input layer and hidden layer are nonlinearly mapped through radial basis functions. The center of the radial basis function is defined as follows:

$$C = P^T \quad (17)$$

$b^1$  represents the threshold of the hidden layer, which is defined as follows:

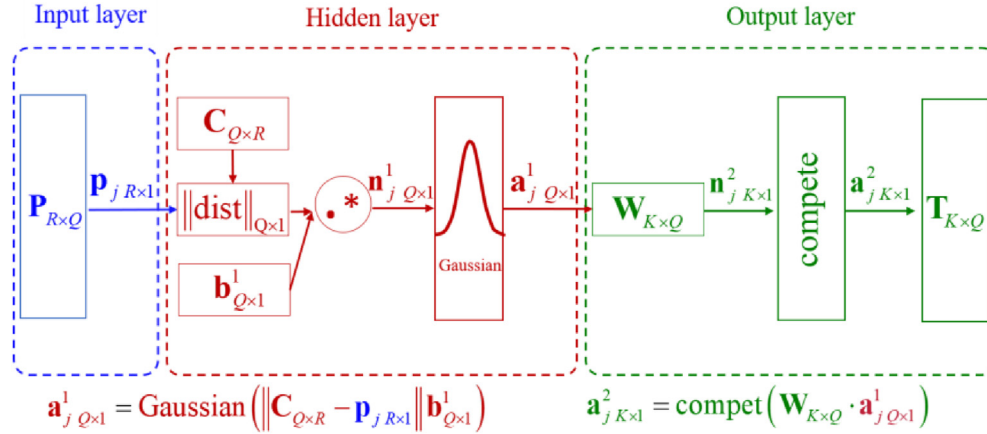


Fig. 5 – Structure diagram of the probabilistic neural network.

$$b^1 = [b^1_1, b^1_2, \dots, b^1_Q]^T \quad (18)$$

where  $b^1_1 = b^1_2 = \dots = b^1_Q = 0.8326$ .

When the center of the radial basis function and the threshold of the hidden layer are determined, the output of the hidden layer neuron can be calculated by Eq. (19):

$$a^1_j = \exp\left(-\frac{(\|C - p_j\| b^1)^2}{\delta^2}\right), \quad j = 1, 2, \dots, Q \quad (19)$$

where  $p_j = [p_{j1}, p_{j2}, \dots, p_{jR}]^T$  represents the  $j^{\text{th}}$  sample in the  $P$ ;  $\|a - b\|$  represents the Euclidean distance between vectors  $a$  and  $b$ ;  $\varphi(x) = \exp\left(-\frac{x^2}{\sigma^2}\right)$  represents the Gaussian function, which is the most commonly used radial basis function.

The output sample  $T$  is taken as the weight factor between the hidden layer and the output layer, which is shown as Eq. (20).

$$W = T \quad (20)$$

### 3) Probabilistic neural network output sample calculation

According to the Parzen method, the output layer neurons estimate the probability of the input samples belonging to various fault codes. The neuron with the largest probability value has an output of 1, and the remaining neurons have an output of 0. The calculation process is described as follows:

$$a^2_j = \text{compet}(W a^1_j) \quad j = 1, 2, \dots, Q \quad (21)$$

### Fault experiment design

Based on the test platform in Fig. 2, EIS data at different fault conditions concerning flooding, drying and reactant starvation can be obtained for model training and testing. As shown in Fig. 6, a flooding fault will occur when the condensation rate of water inside the fuel cell is greater than the evacuation rate.

From the condensation rate perspective, increasing the reactant humidity and the operating current of the fuel cell will increase the partial pressure of water while lowering the temperature will reduce the saturated vapor pressure. As a result, the water condensation rate inside the fuel cell speeds up. On the other hand, undesirably low air stoichiometry, impurities, and manufacturing issues will impair water's evacuation ability. Therefore, the flooding fault can be artificially constructed by changing the four basic controllable parameters (RH, I,  $T_{a/c}$ ) listed in the figure.

Accordingly, the drying fault can be constructed by adjusting the controllable parameters in the opposite direction. Besides, insufficient hydrogen or air in fuel cells may lead to starvation fault during the dynamic conditions of fuel cell vehicles. Compared with the hydrogen supply controlled by the injectors or proportional valves, air starvation is more likely to occur due to the response delay of the air compressor in the vehicular fuel cell system. Promptly adjusting the reacted air mass flow is the most certified method to mitigate the fault. Conversely, different levels of air starvation can be reproduced by sequentially reducing the air stoichiometry.

According to the above analysis, three fault types, namely flooding, membrane drying and air starvation, are set by adjusting the external operating parameters of the fuel cell in this paper, and each fault type is divided into three BFD conditions (minor, moderate and severe). Furthermore, four SFD conditions are set up between the three BFD conditions to test the fault diagnosis performance of the model for arbitrary operating conditions. The EIS is measured 20 times under the BFD conditions and normal conditions (Condition 1 in Table 2, Fault code: 0) and 5 times under the SFD conditions. The operating parameters of fault experiments with different fault types/degrees are displayed in Tables 4–6.

Fig. 7(a)–(c) are the average EIS under the flooding, drying and air starvation conditions. The fault degree is represented by eight Arabic numerals ranging from 0 to 7, where 0 represents the normal condition, 1, 4, 7 correspond to the three BFD conditions (minor, moderate, severe), and 2, 3, 5, 6 correspond to the four SFD conditions. From the fault type perspective, the low-frequency arc radius of the impedance spectra in the flooding fault is larger than that of high-frequency, and the



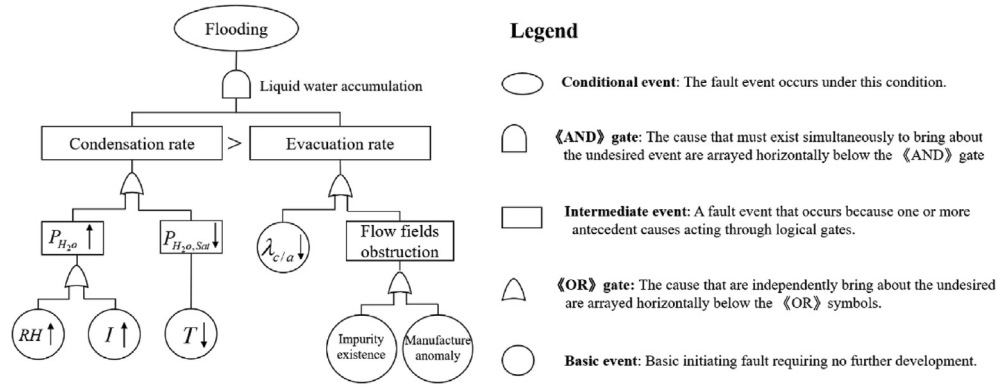


Fig. 6 – Fault tree analysis of fuel cell flooding [41].

Table 4 – Operating parameters for different flooding fault degrees.

Fault degree	Fault Code	Degree Type	$I$ (A/cm <sup>2</sup> )	$P_C/P_A$ (kPa)	$T$ (°C)	$\lambda_C/\lambda_A$	$RH_C/RH_A$
Minor	1	BFD	1.5	150/160	65	2.2/1.5	70%/70%
		SFD	1.55	150/160	65	2.2/1.5	75%/75%
Moderate	2	SFD	1.55	150/160	60	2/1.5	75%/75%
		BFD	1.6	150/160	60	2/1.5	80%/80%
Severe	3	SFD	1.65	150/160	60	2/1.5	85%/85%
		SFD	1.65	150/160	55	1.7/1.5	90%/90%
		BFD	1.7	150/160	55	1.7/1.5	90%/90%

Table 5 – Operating parameters for different drying fault degrees.

Fault degree	Fault Code	Degree Type	$I$ (A/cm <sup>2</sup> )	$P_C/P_A$ (kPa)	$T$ (°C)	$\lambda_C/\lambda_A$	$RH_C/RH_A$
Minor	4	BFD	0.5	150/160	75	2.5/1.5	20%/30%
		SFD	0.5	150/160	75	2.6/1.5	15%/25%
Moderate	5	SFD	0.4	150/160	80	2.6/1.5	15%/25%
		BFD	0.4	150/160	80	2.7/1.5	10%/20%
		SFD	0.4	150/160	80	2.9/1.5	5%/15%
Severe	6	SFD	0.3	150/160	85	2.9/1.5	5%/15%
		BFD	0.3	150/160	85	3/1.5	0%/10%

Table 6 – Operating parameters for different air starvation fault degrees.

Fault degree	Fault Code	Degree Type	$I$ (A/cm <sup>2</sup> )	$P_C/P_A$ (kPa)	$T$ (°C)	$\lambda_C/\lambda_A$	$RH_C/RH_A$
Minor	7	BFD	1	150/160	75	1.7/1.5	50%/60%
		SFD	1	150/160	75	1.65/1.5	50%/60%
Moderate	8	SFD	1	150/160	75	1.55/1.5	50%/60%
		BFD	1	150/160	75	1.5/1.5	50%/60%
		SFD	1	150/160	75	1.45/1.5	50%/60%
Severe	9	SFD	1	150/160	75	1.35/1.5	50%/60%
		BFD	1	150/160	75	1.3/1.5	50%/60%

situation is just the opposite under the drying fault. The same phenomenon also occurs under the air starvation fault, but the difference between the two radii is much larger. The different shapes of the impedance spectra in the three fault types are the premise for judging the fault type of the fuel cell.

From the fault degree perspective, the impedance spectra under the BFD conditions are significantly different, and the impedance spectra under the SFD conditions are closely adjacent to that of the BFD conditions. The SFD conditions are used to test whether the model is effective for any fault

condition between two BFD conditions. Therefore, the SFD conditions should be classified as the corresponding BFD conditions, specifically: fault degree 2 is classified as the minor fault, fault degree 3 and 5 are classified as the moderate fault, and fault degree 6 is classified as the severe fault.

#### Feature parameters determination

Through continuous training, the probabilistic neural network can increase the weight of the effective feature parameters in

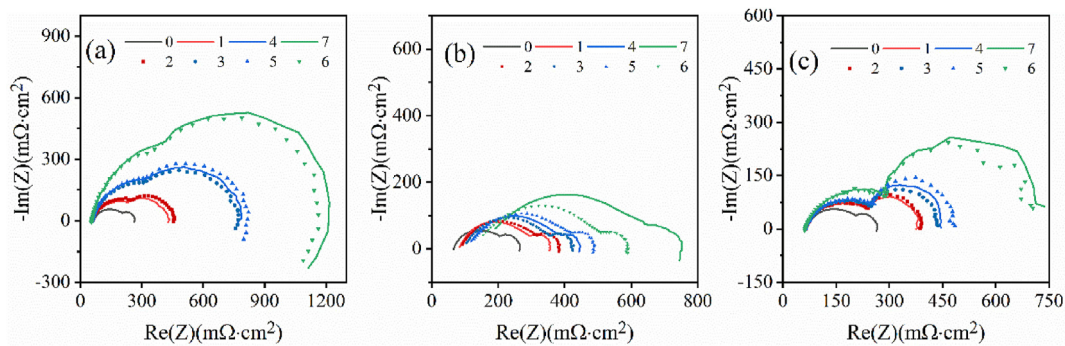


Fig. 7 – Impedance spectra under seven fault degrees: (a) flooding; (b) drying; (c) air starvation.

the input sample and reduce the weight of the interference feature parameters, which means that even if the unprocessed impedance data are input into the model, it can complete the fault diagnosis function as well. However, this results in two problems: a) Increasing numbers of the interference parameter requires more samples to train the probabilistic neural network model; b) High-dimension input samples will inevitably lead to a complex model structure and reduce computational efficiency. Therefore, it is necessary to express the external shape of the impedance spectra with the parameters in the ECM to reduce the dimension of input samples. Furthermore, invalid feature parameters can be eliminated by analyzing the parameter variation with the fault degrees. If a feature parameter does not intersect with each other under the three fault types, it is considered that the parameter can classify the fault types. Analogously, a parameter varying regularly under different fault degrees is considered to have the fault degree diagnostic capability.

Fig. 8(a)–(f) reflects the changes of the seven parameters identified by the RMDE algorithm with the fault degrees. The

fitness function values under all working conditions are less than 0.35 and comparable to the value obtained by Zview, verifying the validity of the identification results.

It can be observed from Fig. 8(a) that the ohmic resistance  $R_s$  has no intersection under the three fault types, which means it has the classification ability of the fault type. The  $R_s$  increases significantly from  $83.85 \text{ m}\Omega\cdot\text{cm}^2$  to  $140.07 \text{ m}\Omega\cdot\text{cm}^2$  as the drying degree increases, while it only slightly decreases under the flooding condition, which reduces from  $60.41 \text{ m}\Omega\cdot\text{cm}^2$  to  $57.13 \text{ m}\Omega\cdot\text{cm}^2$ . Besides, it is not sensitive to the air starvation degree, varies within  $\pm 1 \text{ m}\Omega\cdot\text{cm}^2$  under all the seven degrees. Therefore, the  $R_s$  can classify all the fault types and has the fault degree diagnosis ability under the flooding and drying conditions. As shown in Fig. 8(b), the mass transfer resistance is sensitive to the flooding degree and air starvation degree and increases with the severity in both of the two faults, but it is not sensitive to the drying degree. Since the curves of the air starvation condition and the flooding condition have a large overlap area, single  $R_w$  cannot classify the two fault types and can only classify the drying condition. Fig. 8(c)

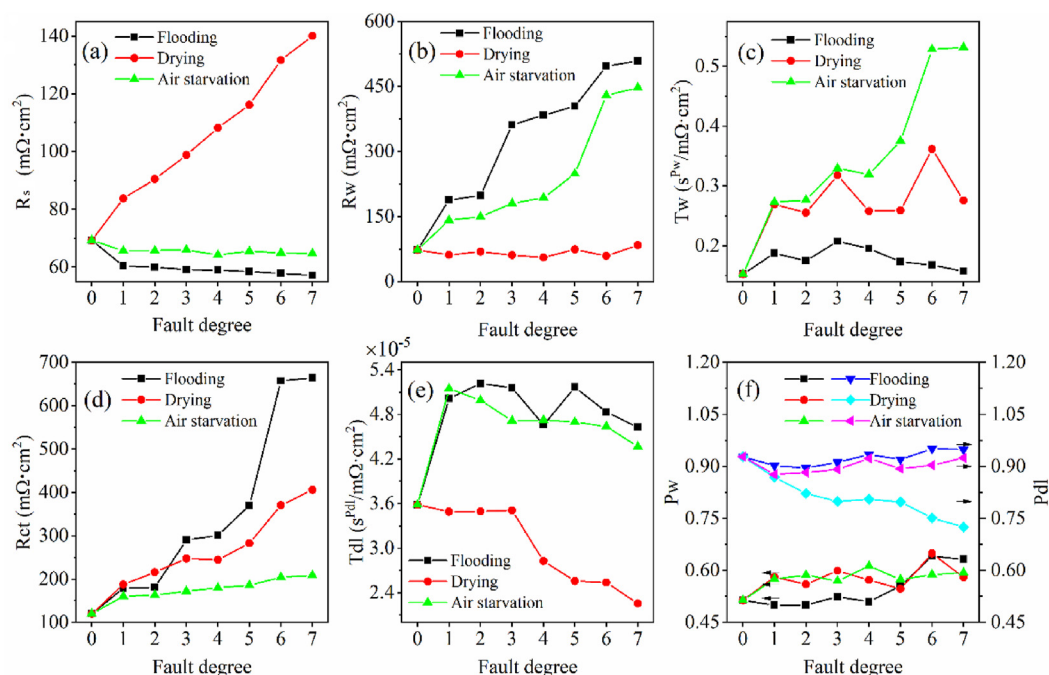


Fig. 8 – Parameter identification results under different operation conditions.

shows that  $T_w$  gradually increases with the air starvation degree, and it does not change regularly under the other two fault types. From the perspective of fault types,  $T_w$  under the flooding condition has no intersection with the other two faults, which is a crucial parameter for identifying the flooding fault. As Fig. 8(d) demonstrates, the polarization resistance  $R_{ct}$  under the three fault types gradually increases with the fault degree. However, the three curves have overlapping areas with each other. Therefore, the  $R_{ct}$  only has the diagnosis ability of the fault degree but cannot classify the fault types. As shown in Fig. 8(e), the pseudo-capacitance  $T_{dl}$  curves under the flooding conditions and air starvation conditions are intertwined. Furthermore, there is no linearity relationship between  $T_{dl}$  and the fault degree under the three faults. Therefore,  $T_{dl}$  does not have the ability to diagnose the fault degree and can only distinguish drying fault from three fault types. Fig. 8(f) demonstrates the variation of CPE exponent  $P_{dl}$  and mass transfer exponent  $P_w$  with different fault degrees. The three  $P_w$  curves are intertwined with each other and stable at 0.55, which is an invalid feature parameter in fault diagnosis. Besides,  $P_{dl}$  is helpful to judge the drying degree, but it has no positive effect in other aspects.

The diagnosis ability of the fault type/degree of the above seven parameters is summarized in Table 7. Define parameters with two or more diagnostic capabilities as the effective feature parameter, namely,  $R_s$ ,  $R_w$ ,  $T_w$ ,  $R_{ct}$  are the four final feature parameters used to fault diagnosis.

#### Validation of the fault diagnosis model

After the feature parameters are selected, 150 sets of randomly selected sample pairs under the BFD conditions are input into the probabilistic neural network model for offline training, and the remaining 50 sets of data under the BFD conditions and 60 sets of data under the SFD conditions are utilized for model testing. The corresponding results are shown in Fig. 9(a) and (b). (Nor, Fl, Dr, and St represent the normal, flooding, drying and air starvation, respectively. Mi, Me, Se represent the minor degree, moderate degree and severe degree.)

It can be seen from Fig. 9(a) that the model gives excellent diagnosis results under the BFD conditions, and the diagnosis accuracies for the fault type/degree are both 100%. The reason for this is that both the training and test data are derived from

**Table 7 – Fault classification capability of the identified parameters in ECM.**

Function	Mode	$R_s$	$R_w$	$T_w$	$P_w$	$R_{ct}$	$T_{dl}$	$P_{dl}$
Fault classify	Flooding	Y	N	Y	N	N	N	N
	Drying	Y	Y	N	N	N	Y	N
	Air starvation	Y	N	N	N	N	N	N
Degree classify	Flooding	Y	Y	N	N	Y	N	N
	Drying	Y	N	N	N	Y	N	Y
	Air starvation	N	Y	Y	N	Y	N	N

Note: Y represents the parameter has the ability, N is not.

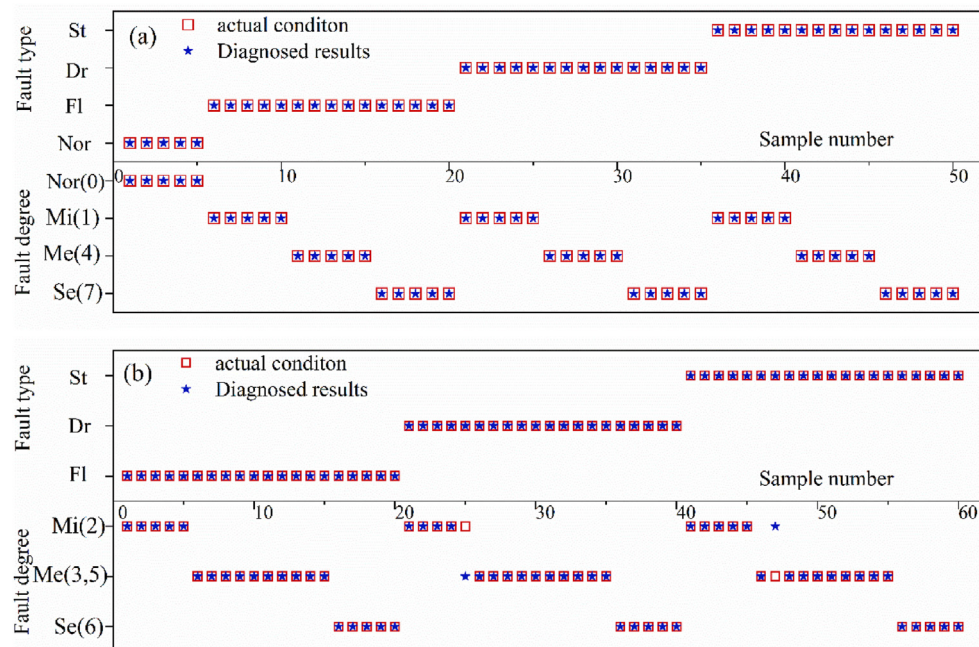


**Fig. 9 – Fault diagnosis results: (a) diagnosis results under the BFD conditions; (b) diagnosis results under the SFD conditions.**

impedance parameters under the BFD conditions, and the trained model has been very sensitive to the external features of these data after the thorough adjustment of the weight parameters in the diagnosis model.

Fig. 9(b) demonstrates the model testing results under the SFD conditions. From the fault type perspective, the model still has a strong classification performance of fault type due to the significant difference in feature parameters, and the classification accuracy of fault type reaches 100%. In terms of fault degree, the model has two sets of misjudgment in the 25th sample and the 47th sample, and the accuracy for the fault degree is 96.67%. The real fault degrees of the two samples are fault degree 2 and fault degree 3. They are both between the basic minor degree and the basic moderate degree. Therefore, it is reasonable to believe that the fault degree misjudgment results from the subtle changes in the impedance spectra shape caused by the internal instability of the fuel cell.

The results indicate that the diagnosis model has a powerful fault type classification capability by subdividing each fault type into three fault degrees, thus avoiding the fault type confusion phenomenon. In addition, it should be noted that the diagnosis model is essentially a data-driven approach and the diagnosis accuracy strongly depends on the structural characteristics of the data to be tested. The impedance spectra measured under part of the SFD conditions in this study are close to the impedance spectra under BFD conditions, especially obvious under flooding conditions, which is the primary reason for the high accuracy under SFD conditions. EIS experiments with more refined operating parameters were not performed, but it can be reasonably inferred that the diagnosis model may make a fault degree misjudgment if the impedance spectrum to be tested is exactly in the middle of the impedance spectra of two BFD conditions. However, it is almost impossible for the model to produce a fault type misjudgment after trained with the data from the different fault types/degrees. In a word, the diagnosis scheme in this paper to refine the fault degree based on the fault type can effectively eliminate the fault type confusion and enhance the fuel cell system reliability.

## Conclusions

This study proposes a probabilistic neural network-based fault diagnosis model to diagnose the fuel cell fault type and fault degree. Main works can be summarized as follows:

A parameter identification method based on the RMDE algorithm is proposed. Firstly, an improved Randles ECM is developed to denote the different voltage loss of the fuel cell. Then, an RMDE algorithm-based parameter identification method is presented to achieve the parameters identification. The identification results under four different conditions demonstrate that the difference between the parameters identified by the RMDE algorithm and Zview is within 4.5%. The algorithm runs ten times consecutively, and all the results converge to the same stable value within 3 s, indicating that it has strong robustness and fast convergence speed.

A probabilistic neural network-based diagnosis model is developed for the fault diagnosis of the fuel cell. Based on the

changing law of the parameters under the BFD and SFD conditions, four parameters are selected as valid feature parameters to be input into the probabilistic neural network-based fault diagnosis model. The model accurately diagnoses the fault types and fault degree under the BFD conditions and achieves the diagnosis accuracy of 100%. Under the SFD conditions, the model still has a strong classification performance for the fault type, and the accuracy reaches 100% in the tests. As for fault degree, the model has two sets of misjudgment in the 25th sample and the 47th sample, and the overall accuracy for the fault degree is 96.67%. In conclusion, the fault diagnosis model reduces the probability of fault type confusion and is an effective means to enhance the reliability of the fuel cell system.

## Declaration of competing interest

The authors declare that they have no known competing financial interests or personal relationships that could have appeared to influence the work reported in this paper.

## Acknowledgement

This work was supported by National Key Research and Development Program of China (Funding Number: 2019YFB1504605, 2018YFB0106502).

## REFERENCES

- [1] Wang G, Yu Y, Liu H, Gong C, Wen S, Wang X, et al. Progress on design and development of polymer electrolyte membrane fuel cell systems for vehicle applications: a review. *Fuel Process Technol* 2018;179:203–28. <https://doi.org/10.1016/j.fuproc.2018.06.013>.
- [2] Das V, Padmanaban S, Venkitesamy K, Selvamuthukumaran R, Blaabjerg F, Siano P. Recent advances and challenges of fuel cell based power system architectures and control – a review. *Renew Sustain Energy Rev* 2017;73:10–8. <https://doi.org/10.1016/j.rser.2017.01.148>.
- [3] Yuan X-Z, Li H, Zhang S, Martin J, Wang H. A review of polymer electrolyte membrane fuel cell durability test protocols. *J Power Sources* 2011;196:9107–16.
- [4] Sutharssan T, Montalvao D, Chen YK, Wang W-C, Pisac C, Elemara H. A review on prognostics and health monitoring of proton exchange membrane fuel cell. *Renew Sustain Energy Rev* 2017;75:440–50. <https://doi.org/10.1016/j.rser.2016.11.009>.
- [5] Wu J, Yuan XZ, Wang H, Blanco M, Martin JJ, Zhang J. Diagnostic tools in PEM fuel cell research: Part I Electrochemical techniques. *Int J Hydrogen Energy* 2008;33:1735–46. <https://doi.org/10.1016/j.ijhydene.2008.01.013>.
- [6] Wu J, Zi Yuan X, Wang H, Blanco M, Martin JJ, Zhang J. Diagnostic tools in PEM fuel cell research: Part II: physical/chemical methods. *Int J Hydrogen Energy* 2008;33:1747–57. <https://doi.org/10.1016/j.ijhydene.2008.01.020>.
- [7] Tang Z, Huang Q-A, Wang Y-J, Zhang F, Li W, Li A, et al. Recent progress in the use of electrochemical impedance spectroscopy for the measurement, monitoring, diagnosis



- and optimization of proton exchange membrane fuel cell performance. *J Power Sources* 2020;468:228361. <https://doi.org/10.1016/j.jpowsour.2020.228361>.
- [8] Wang X, Wei X, Zhu J, Dai H, Zheng Y, Xu X, et al. A review of modeling, acquisition, and application of lithium-ion battery impedance for onboard battery management. *eTransportation* 2021;7:100093. <https://doi.org/10.1016/j.etrans.2020.100093>.
  - [9] Rezaei Niya SM, Phillips RK, Hoorfar M. Study of anode and cathode starvation effects on the impedance characteristics of proton exchange membrane fuel cells. *J Electroanal Chem* 2016;775:273–9. <https://doi.org/10.1016/j.jelechem.2016.06.013>.
  - [10] Chevalier S, Josset C, Bazylak A, Auvity B. Measurements of air velocities in polymer electrolyte membrane fuel cell channels using electrochemical impedance spectroscopy. *J Electrochem Soc* 2016;163:F816–23. <https://doi.org/10.1149/2.0481608jes>.
  - [11] Hink S, Roduner E. Application of a contact mode AFM for spatially resolved electrochemical impedance spectroscopy measurements of a Nafion membrane electrode assembly. *Phys Chem Chem Phys* 2013;15:1408–16. <https://doi.org/10.1039/c2cp42843a>.
  - [12] Antonacci P, Chevalier S, Lee J, Yip R, Ge N, Bazylak A. Feasibility of combining electrochemical impedance spectroscopy and synchrotron X-ray radiography for determining the influence of liquid water on polymer electrolyte membrane fuel cell performance. *Int J Hydrogen Energy* 2015;40:16494–502. <https://doi.org/10.1016/j.ijhydene.2015.10.008>.
  - [13] Bender G, Angelo M, Bethune K, Dorn S, Thampan T, Rocheleau R. Method using gas chromatography to determine the molar flow balance for proton exchange membrane fuel cells exposed to impurities. *J Power Sources* 2009;193:713–22. <https://doi.org/10.1016/j.jpowsour.2009.04.028>.
  - [14] Boillat P, Lehmann EH, Trtik P, Cochet M. Neutron imaging of fuel cells – recent trends and future prospects. *Current Opinion in Electrochemistry* 2017;5:3–10. <https://doi.org/10.1016/j.coelec.2017.07.012>.
  - [15] Hong P, Xu L, Jiang H, Li J, Ouyang M. A new approach to online AC impedance measurement at high frequency of PEM fuel cell stack. *Int J Hydrogen Energy* 2017;42:19156–69. <https://doi.org/10.1016/j.ijhydene.2017.06.035>.
  - [16] Nonobe, YJITo Electrical, Engineering E. Development of the fuel cell vehicle mirai, 12; 2017. p. 5–9.
  - [17] Zheng Z, Petrone R, Péra MC, Hissel D, Becherif M, Pianese C, et al. A review on non-model based diagnosis methodologies for PEM fuel cell stacks and systems. *Int J Hydrogen Energy* 2013;38:8914–26. <https://doi.org/10.1016/j.ijhydene.2013.04.007>.
  - [18] Petrone R, Zheng Z, Hissel D, Péra MC, Pianese C, Sorrentino M, et al. A review on model-based diagnosis methodologies for PEMFCs. *Int J Hydrogen Energy* 2013;38:7077–91. <https://doi.org/10.1016/j.ijhydene.2013.03.106>.
  - [19] Yuan H, Dai H, Wei X, Ming P. Model-based observers for internal states estimation and control of proton exchange membrane fuel cell system: a review. *J Power Sources* 2020;468:228376. <https://doi.org/10.1016/j.jpowsour.2020.228376>.
  - [20] Benmouna A, Becherif M, Depernet D, Gustin F, Ramadan HS, Fukuhara S. fault diagnosis methods for proton exchange membrane fuel cell system. *Int J Hydrogen Energy* 2017;42:1534–43. <https://doi.org/10.1016/j.ijhydene.2016.07.181>.
  - [21] Rubio MA, Urquía A, Dormido S. Diagnosis of performance degradation phenomena in PEM fuel cells. *Int J Hydrogen Energy* 2010;35:2586–90. <https://doi.org/10.1016/j.ijhydene.2009.03.054>.
  - [22] Yuan H, Dai H, Wei X, Ming P. A novel model-based internal state observer of a fuel cell system for electric vehicles using improved Kalman filter approach. *Appl Energy* 2020;268:115009. <https://doi.org/10.1016/j.apenergy.2020.115009>.
  - [23] Buchholz M, Eswein M, Krebs V. Ieee. Modelling PEM fuel cell stacks for FDI using linear subspace identification. 2008 IEEE international conference on control applications, vols. 1 and 2. New York: Ieee; 2008. p. 363–8.
  - [24] Li Z, Outbib R, Giurgea S, Hissel D, Giraud A, Couderc P. Fault diagnosis for fuel cell systems: a data-driven approach using high-precise voltage sensors. *Renew Energy* 2019;135:1435–44. <https://doi.org/10.1016/j.renene.2018.09.077>.
  - [25] Mao L, Jackson L, Huang W, Li Z, Davies B. Polymer electrolyte membrane fuel cell fault diagnosis and sensor abnormality identification using sensor selection method. *J Power Sources* 2020;447:227394. <https://doi.org/10.1016/j.jpowsour.2019.227394>.
  - [26] Li ZL, Outbib R, Giurgea S, Hissel D. Diagnosis for PEMFC systems: a data-driven approach with the capabilities of online adaptation and novel fault detection. *IEEE Trans Ind Electron* 2015;62:5164–74. <https://doi.org/10.1109/tie.2015.2418324>.
  - [27] Pahon E, Yousfi Steiner N, Jemei S, Hissel D, Moçoteguy P. A signal-based method for fast PEMFC diagnosis. *Appl Energy* 2016;165:748–58. <https://doi.org/10.1016/j.apenergy.2015.12.084>.
  - [28] Lu H, Chen J, Yan C, Liu H. On-line fault diagnosis for proton exchange membrane fuel cells based on a fast electrochemical impedance spectroscopy measurement. *J Power Sources* 2019;430:233–43. <https://doi.org/10.1016/j.jpowsour.2019.05.028>.
  - [29] Wang X, Li Q, Wang T, Liu J, Jiang L, Chen W. EIS measurement based on DIBS excitation signal and fault diagnosis method of fuel cell. *Proceedings of the CSEE* 2020;40. <https://doi.org/10.13334/j.0258-8013.pcsee.191043.4526-4537+732>.
  - [30] Risse S, Cañas NA, Wagner N, Härk E, Ballauff M, Friedrich KA. Correlation of capacity fading processes and electrochemical impedance spectra in lithium/sulfur cells. *J Power Sources* 2016;323:107–14. <https://doi.org/10.1016/j.jpowsour.2016.05.032>.
  - [31] Wei B, Xie N. Parameter estimation for grey system models: a nonlinear least squares perspective. *Commun Nonlinear Sci Numer Simulat* 2020;105653. <https://doi.org/10.1016/j.cnsns.2020.105653>.
  - [32] Wang X. Nonlinear model parameter estimation. 1 ed. Wuhan: Wuhan University Press; 2002.
  - [33] Fouquet N, Doulet C, Nouillant C, Dauphin-Tanguy G, Ould-Bouamama B. Model based PEM fuel cell state-of-health monitoring via ac impedance measurements. *J Power Sources* 2006;159:905–13. <https://doi.org/10.1016/j.jpowsour.2005.11.035>.
  - [34] Girault HH, Deslouis C. *Electrochimie Physique et analytique*. Presses Polytechniques et Universitaires Romandes; 2001.
  - [35] Wang Q, He Y, Shen J, Hu X, Ma Z. State of charge-dependent polynomial equivalent circuit modeling for electrochemical impedance spectroscopy of lithium-ion batteries. *IEEE Trans Power Electron* 2018;33:8449–60. <https://doi.org/10.1109/TPEL.2017.2780184>.
  - [36] Wang X, Wei X, Dai H. Estimation of state of health of lithium-ion batteries based on charge transfer resistance considering different temperature and state of charge. *J Energy Storage* 2019;21:618–31. <https://doi.org/10.1016/j.est.2018.11.020>.

- 
- [37] Qin AK, Huang VL, Suganthan PN. Differential evolution algorithm with strategy adaptation for global numerical optimization. *IEEE Trans Evol Comput* 2009;13:398–417. <https://doi.org/10.1109/TEVC.2008.927706>.
- [38] Chang CS, Xu DY. Differential evolution based tuning of fuzzy automatic train operation for mass rapid transit system. *IEE Proc Elec Power Appl* 2000;147:206–12. <https://doi.org/10.1049/ip-epa:20000329>.
- [39] Mendes R, Mohais AS. DynDE: a differential evolution for dynamic optimization problems. 2005. *IEEE Congress on Evolutionary Computation* 2005;3:2808–15.
- [40] Pivac I, Barbir F. Inductive phenomena at low frequencies in impedance spectra of proton exchange membrane fuel cells – a review. *J Power Sources* 2016;326:112–9. <https://doi.org/10.1016/j.jpowsour.2016.06.119>.
- [41] Yousfi-Steiner N, Moçotéguy P, Candusso D, Hissel D, Hernandez A, Aslanides A. A review on PEM voltage degradation associated with water management: impacts, influent factors and characterization. *J Power Sources* 2008;183:260–74. <https://doi.org/10.1016/j.jpowsour.2008.04.037>.